Biomechanical effects of hyper-dynamic cerebrospinal fluid flow through the cerebral aqueduct in idiopathic normal pressure hydrocephalus patients

Shusaku Maeda[1], Tomohiro Otani[1], Shigeki Yamada[2,3,4], Yoshiyuki Watanabe[3], Selin Yavuz Ilik[1], Shigeo Wada[1]

1 Graduate School of Engineering Science, Osaka University, 1-3 Machikaneyamacho, Toyonaka, Osaka, 560-8531, Japan

2 Department of Neurosurgery, Nagoya City University Graduate School of Medical Science, 1 Kawasumi, Mizuho-cho, Mizuho-ku, Nagoya, Aichi, 467-8601, Japan

3 Interfaculty Initiative in Information Studies / Institute of Industrial Science, The University of Tokyo, Tokyo, Japan

4 Department of Neurosurgery, Shiga University of Medical Science, Setatsukinowacho, Otsu, Shiga, 520-2192, Japan

5 Department of Radiology, Shiga University of Medical Science, Setatsukinowacho, Otsu, Shiga, 520-2192, Japan

Type: Original Article

Address for Correspondence:

Tomohiro Otani, PhD

Department of Mechanical Science and Bioengineering,

Graduate School of Engineering Science, Osaka University

1-3 Machikaneyamacho, Toyonaka, Osaka, 560-8531, Japan

Phone: +81-6-6850-6174

E-mail: otani.tomohiro.es@osaka-u.ac.jp

Keywords: Cerebrospinal fluid, Brain ventricle, Magnetic resonance imaging, Computational fluid dynamics, Flow mixing.

Word count: 3500

Abstract

Normal pressure hydrocephalus (NPH) is an intracranial disease characterized by an abnormal accumulation of cerebrospinal fluid (CSF) in brain ventricles within the normal range of intracranial pressure. Most NPH in aged patients is idiopathic (iNPH) and without any prior history of intracranial diseases. Although an abnormal increase of the CSF stroke volume (hyper-dynamic CSF flow) in the aqueduct between the third and fourth ventricles in iNPH patients has received much attention as a clinical evaluation index, biomechanical effects of this flow on iNPH pathophysiology are poorly understood. This study aimed to clarify the potential biomechanical effects of hyper-dynamic CSF flow through the aqueduct of iNPH patients using magnetic resonance imaging-based computational simulations. Ventricular geometries and CSF flow rates through aqueducts of 10 iNPH patients and 10 healthy control subjects were obtained from multimodal magnetic resonance images, and these CSF flow fields were simulated using computational fluid dynamics. As biomechanical factors, we evaluated the wall shear stress on the ventricular wall and the extent of flow mixing, which potentially disturbs the CSF composition in each ventricle. The results showed that the relatively high CSF flow rate and large and irregular shapes of the aqueduct in iNPH resulted in large wall shear stresses localized in relatively narrow regions. Furthermore, the resulting CSF flow showed stable cyclic motion in control subjects, whereas strong mixing during transport was found through the aqueduct in patients with iNPH. These findings provide further insights into the clinical and biomechanical correlates of NPH pathophysiology.

1 Introduction

Cerebrospinal fluid (CSF) fills brain ventricles and subarachnoid spaces and enables homeostatic transport of nutrients and hormones (May et al., 1990). Abnormal accumulation of CSF in the ventricles within normal ranges of intracranial pressure is called normal pressure hydrocephalus (NPH; Marmarou et al., 2005) and causes multiple dysfunctions, such as cognitive impairment, gait disturbance, and urinary incontinence (Mori et al., 2012). In particular, idiopathic NPH (iNPH) is a major form of NPH observed in aged patients without prior history of intracranial disease. Because of its association with aging and cognitive dysfunction (Nakajima et al., 2021), the etiology and pathophysiology of iNPH have received much attention from medical (Zhangyang et al., 2020) and biomechanical (Linninger et al., 2016) researchers.

Hyper-dynamic CSF flow in the aqueduct (the flow pathway through the third and fourth ventricles) has been widely reported in phase-contrast magnetic resonance imaging (PCMRI) studies of iNPH patients as a part of disease progression (Bradley et al., 1996; Scollato et al., 2008; Shanks et al., 2019). CSF flow in the aqueduct is pulsatile and bidirectional, synchronizing with cerebral arterial expansion during the cardiac cycle (Bradley et al., 1996; Brinker et al., 2014; Enzmann et al., 1993). However, characterization of hyper-dynamic CSF flow through the aqueduct has been limited to a clinical diagnostic index, and the associations of biomechanical effects with intracranial homeostasis and pathophysiology are poorly understood.

This study considered two biomechanical effects of the hyper-dynamic CSF flow through the aqueduct in iNPH patients. The first is an abnormal mechanical stimulus against the ependymal cells lining the aqueduct lumens. Since malfunction of the motile cilia of the ependymal cells

occurs during hydrocephalus (Lechtreck et al., 2008; Shook et al., 2014), greater CSF flow may result in a physiologically inappropriate mechanical stimulus on the ependymal cells and affect their functions (Yamada et al., 2021). The second biomechanical effect is an abnormal mixing of CSF between third and fourth ventricles through the aqueduct. The CSF contains proteins and signaling molecules in the form of actively released neuroactive substances (Nicholson, 1999; Skipor and Thiery, 2008), which are mainly produced by the epithelium of the choroid plexus located in each ventricle (Damkier et al., 2013): the CSF composition varies among the ventricles in normal conditions (Cavanagh et al., 1983; Lun et al., 2015; Zappaterra et al., 2007). Abnormal mixing of CSF compositions has been observed in the ventricular and subarachnoid spaces (Ringstad et al., 2017) and lumbar and ventricular regions (Puy et al., 2016) in iNPH patients. These abnormalities in CSF flow and the chemical environment of the CSF have been associated with depression, cognitive dysfunction, and nervous system disorders (Attier-Zmudka et al., 2019; Bothwell et al., 2019; Seo et al., 2021). These findings suggest that mixing of CSF through aqueducts disturbs the individual CSF compositions of the third and fourth ventricles and is associated with pathologic conditions. We therefore hypothesized that hyper-dynamic CSF flow through the aqueduct has potential biomechanical effects on intracranial homeostasis. Understanding these effects may link characteristic CSF flow profiles observed in clinical practice with existing biomechanical knowledge regarding iNPH pathophysiology.

This study aimed to clarify the biomechanical effects of hyper-dynamic CSF flow through the cerebral aqueduct between the third and fourth ventricles of iNPH patients by combining MRI measurements and computational simulations. Subject-specific ventricle geometries and aqueduct flow rates were acquired from T2-weighted MRI and four-dimensional (4D) flow MRI

measurements, respectively, of 10 iNPH patients and 10 healthy controls. Based on these data, computational fluid dynamics simulations of CSF flow in the ventricles of each patient were conducted. The mechanical effects of normal CSF flow and CSF flow mixing on the ventricle were analyzed using the CSF flow velocity field obtained from computational simulations.

2 Materials and Methods

2.1 Study participants

Participants included 10 iNPH patients (six male, four female; age range, 61–83 y; iNPH1–iNPH10) diagnosed following the Japanese clinical guidelines for iNPH (Nakajima et al., 2021) and 10 healthy controls (seven male, three female; age range, 22–47 y; control1–control10) who received treatment at the Department of Neurosurgery, Shiga University of Medical Science Hospital in 2018–2021. Inclusion criteria for iNPH patients and healthy controls are described in Supplementary 1. The study was approved by the Institutional Review Boards of Shiga University of Medical Science (No. R2019-227) and Osaka University (No. R2-1). Patients were included after they gave oral and written informed consent.

Image acquisition was performed for each subject using a 3-T MRI scanner (Discovery MR 750W, GE Healthcare, Milwaukee, WI, USA). Three-dimensional velocity-encoded data were obtained using the 4D flow MRI sequence with 5 cm/s velocity encoding (0.7813 mm × 0.7813 mm × 1.0 mm) and eight phases of the cardiac cycle were reconstructed. Furthermore, to construct patient-specific geometries of the brain ventricles, we used volumetric data obtained from a T2-weighted sequence (0.8 mm × 0.8 mm × 0.8 mm). Measurement details are shown in Supplementary 2.

2.2 Image processing

Ventricle geometries were extracted from T2-weighted MRI data and reconstructed as a set of triangular surfaces using Mimics (Version 23; Materialize Inc., Yokohama, Japan). Table 1 shows basal geometric properties of the aqueduct and ventricles in all patients, in which the measurement protocol is shown in Supplementary 3. Representative geometries of controls and iNPH patients are shown in Fig. 1(A) and (B), and variations in the aqueduct cross-sectional area are summarized in Fig. 1(C). In controls, the aqueduct cross-sectional area monotonically decreased from the fourth to the third ventricle and ranged from 1.67 to 39.0 mm^2. In contrast, the corresponding area in iNPH patients had a local minimum near the center of the aqueduct and relatively large variation ranging from 2.34 to 46.8 mm^2. The absolute minimum aqueduct diameter was 1.46 mm and 2.32 mm in controls and iNPH patients, respectively.

Next, the time course of the CSF flow rate through the aqueduct was obtained using 4D flow MRI. Aliasing artifacts and eddy-current-based phase offsets were eliminated following the methods used in our previous study (Yavuz Ilik et al., 2022). To consider the characteristic features of CSF flow in the aqueduct, we computed the Reynolds number ($\mathrm{Re} = \rho UD / \mu$) and Womersley number ($\mathrm{Wo} = D\left(\omega\rho / \mu\right)^{\frac{1}{2}}$) as non-dimensional indices, where ρ is the density, μ is the viscosity, U is average velocity through the aqueduct cross-section, ω is the circular frequency of oscillatory flow in the aqueduct calculated from the cardiac cycle, and *D* is the equivalent diameter of the aqueduct cross-section. Following experimental data, we defined ρ = 1×10^3 kg/m^3 and μ = 1×10^{-3} Pa·s (Bloomfield et al., 1998). Validities of the 4D flow MRI data was confirmed in Appendix 1.

2.3 Numerical simulation

CSF domains were spatially discretized using first-order tetrahedral elements with a base mesh size of 0.7 mm and three layers of boundary prism layer elements using ICEM CFD (Version 2021 R2; ANSYS Inc., Canonsburg, USA). The mesh size independency test was conducted as noted in Supplementary 4. The CSF was modeled as an incompressible Newtonian fluid based on existing experimental data (Bloomfield et al., 1998). We modeled the CSF flow as being driven by arterial pulsations without CSF production because the influence of CSF production is relatively small over this time scale (Bradley, 2015). On the basis of this assumption, we expressed CSF flow as a transient volume change in the lateral ventricles (LVs) equivalent to the aqueduct flow rate. Thus, CSF flow was expressed by the equation of continuity and incompressible Navier–Stokes equation in arbitrary Lagrangian–Eulerian form for moving-wall boundary problems, given by

$$\nabla \cdot \mathbf{v} = 0\,, \tag{1}$$

$$\rho\left(\partial_t \mathbf{v} + \tilde{\mathbf{v}} \cdot \nabla \mathbf{v}\right) = -\nabla p + \mu \nabla^2 \mathbf{v}\,, \tag{2}$$

where $\mathbf{v}$ is the velocity vector, $\tilde{\mathbf{v}}$ is the advection velocity in the arbitrary Lagrangian–Eulerian coordinates, and p is the pressure. These equations were spatially discretized in a finite element manner using a streamline upwind Petrov–Galerkin formulation (Bazilevs et al., 2012) and computed by fractional step method. Computational details are briefly introduced in Supplementary material 5.

Regarding computational conditions, we set prescribed moving-wall boundary conditions on the LV surface. The LV motion was simplified by assuming isotropic volume expansion and contraction, and the rate of the LV volume change was set to the aqueduct flow rate measured

158 using 4D flow MRI (Fig. 2(A)), following Sweetman et al. (2011). Uniform displacement was
159 assigned on each LV surface node and its direction was set to unit surface normal. Cut-sections of
160 the foramen of Magendie and foramen of Luschka were set to a fixed pressure boundary
161 condition of 0 Pa. The time increment was set to 1×10^{-3} s to satisfy a Courant–Friedrichs–Lewy
162 number < 0.15. Computational simulations were conducted through four cardiac cycles for each
163 subject. In section 3, we show results from the fourth cardiac cycle unless otherwise noted.

164 **2.4 Evaluation indices**

165 First, we evaluated spatial distributions of wall shear stress (WSS) on the aqueduct surface
166 at the time of maximum CSF flow rate from the third to fourth ventricles to consider mechanical
167 stimulus associated with the hyper-dynamic CSF flow. Following previously described methods,
168 WSS was computed in each element using the shear stress tensor $\frac{1}{2}\mu\left(\nabla\mathbf{v}^{\top}+\nabla\mathbf{v}\right)$ and surface
169 unit normal (Sotelo et al., 2015). Next, we evaluated CSF flow mixing through the aqueduct using
170 massless particle tracers. The tracers were positioned at intervals of 0.25 mm along the aqueduct
171 with respect to each direction in Cartesian coordinates, and their motions were tracked through
172 20 cardiac cycles. Particle motions were expressed using the flow velocity vector $\mathbf{v}$, given by

173 $$\frac{d\mathbf{x}_i}{dt} = \mathbf{v}, \tag{3}$$

174 where $\mathbf{x}_i$ is the position vector of the particle i. Eq. (3) was iteratively solved using the fourth-
175 order Runge–Kutta method. For quantitative evaluation of the mixing using these particle tracers,
176 we computed the mix-norm (Mathew et al., 2005) adjusted for discrete particle mixing as
177 described by Arzani et al. (2014). The mix-norm is a multi-scale mixing index that assesses the

mixing extent and ranges from zero (not mixed) to one (completely mixed). A brief definition and computation of the mix-norm are shown in Appendix 2 for completeness. To compute the mix-norm, the approximate shape of the aqueduct was defined from the reconstructed surface as a domain between the third and fourth ventricles with a diameter less than twice the minimum diameter. Differences in the anatomical and physical data between iNPH patients and control subjects were assessed statistically using the Mann–Whitney *U* test (SciPy v1.6.2 software; https://scipy.org/).

3 Results

Figure 2(A) shows the time courses of CSF flow rate (A) in the aqueduct on 4D flow MRI. Flow from the fourth to the third ventricle was deemed positive and the cardiac cycle was considered to start at early systole. The flow rate showed a pulsatile motion with a negative value in systole and a positive value in diastole. The maximum flow rate in iNPH patients was approximately three-fold higher than that in controls ($p < 5 \times 10^{-3}$). Figure 2(B) and (C) showed the maximum Re and Wo. Significant differences of these both numbers were found between iNPH patients (Re: 58.0 ± 27.6, Wo: 0.86 ± 0.14) and controls (Re: 13.7±8.3, Wo: 1.50 ± 0.32) (Re: $p < 1 \times 10^{-3}$ and Wo: $p < 5 \times 10^{-4}$).

Figure 3 shows WSS spatial distributions on the aqueduct surface in representative control and iNPH cases (iNPH2, control1). WSS magnitudes were almost constant in controls (Fig. 3(A)), whereas high WSS values were found in relatively narrow domains in iNPH (Fig. 3(B)). For quantitative comparisons of these tendencies, we computed WSS distributions along the longitudinal direction of the aqueduct. The average WSS magnitude ranged from 8 to 25 mPa in

199 controls, whereas that in iNPH patients was approximately three-fold higher and ranged from 23
200 to 78 mPa ($p = 1.7\times10^{-3}$). Furthermore, spatial variations of the WSS magnitude in iNPH patients
201 were 5–6-fold larger than those in controls, and stresses were localized in the center region with
202 relatively narrow cross-sections. CSF stroke volumes and peak WSS magnitudes are summarized
203 in Supplementary 6.

204 The CSF mixing states in the aqueduct were analyzed using massless particle tracing through
205 20 cardiac cycles. Figure 4 shows representative snapshots of the particle tracer distributions
206 from the initial state to fourth cardiac cycle in the aqueduct in control1 and iNPH2. In controls,
207 the particle tracer showed a slight but steady cyclic motion (Supplementary 7). In contrast, in
208 iNPH patients, relatively strong mixing with particle transfers between ventricles through the
209 aqueduct was found (Supplementary 8).

210 Figure 5 illustrates the particle tracer distributions in all subjects after 20 cardiac cycles. The
211 particle distribution remained almost the same as that in the initial setting in all controls, while
212 the distribution in iNPH patients showed notable variety and mixing, especially in iNPH2 and
213 iNPH8. In these cases, particle tracers were cyclically moved following CSF convection
214 synchronized with the cardiac cycle and gradually drifted from their initial positions. Particles
215 located in the third ventricles reached the fourth ventricle through the aqueduct within 20
216 cardiac cycles, and vice versa. We computed the mix-norm in each subject for the quantitative
217 evaluation of the CSF mixing state from particle tracers in the aqueduct. Figure 6 shows the time
218 courses of the mix-norm in the aqueduct in all participants. In the controls, the mix-norm
219 moderately increased and remained under 0.5 in all cases even after 20 cardiac cycles. In contrast,
220 iNPH patients tended to have a steep increase and wide patient-specific variation of the mix-

norm from 0.2 to 0.9 after 20 cardiac cycles. The median values of the mix-norm after 20 cardiac cycles were 0.314 and 0.523 in controls and iNPH patients, respectively, and these values were significantly different ($p = 7 \times 10^{-3}$).

4 Discussion

The hyper-dynamic CSF flow through the aqueduct between third and fourth ventricle is widely known as a part of iNPH progression (Scollato et al., 2008), while these the biomechanical effect of the hyper-dynamic CSF flow remains unclear. To address this issue, this study investigated CSF flow dynamics through the aqueduct in iNPH patients and control subjects using MRI-based computational simulations. MRI showed that iNPH patients have characteristic properties, including large ventricles, as summarized in the clinical guideline (Nakajima et al., 2021), and a relatively high CSF flow rate (Fig. 2), consistent with existing clinical reports (Bradley, 2015). Based on these MRI measurements, the CSF flow dynamics in each patient were determined using computational simulations, and biomechanical properties, such as wall shear stress and flow mixing, were evaluated.

To consider the size of the mechanical stimulus associated with the CSF flow enhancements, we evaluated the peak WSS on the aqueduct surface. Although WSS analyses on the aqueduct surface have been performed using images from 4D flow MRI (e.g., Yamada et al., 2020, 2021), there are strong severe concerns about their accuracy because of limitations in spatial resolution and use of eddy-current-based offsets to measure small flow velocities (Wentland et al., 2010), which needs appropriate offset eliminations (e.g., Yavuz Ilik et al., 2022) to address the above concerns and obtain reasonable WSS profiles. The obtained results showed that iNPH causes not

only approximately 3-fold larger base WSS values compared with control subjects but also 5–6-fold larger WSS variations (Fig. 3) associated with the geometric alteration shown in Fig. 1. These differences indicate that ependymal cells on the aqueduct surface are exposed to abnormal local mechanical stimuli in iNPH. Because the relatively large WSS causes damage to the ependymal cells with loss of the motile cilia and this damage associates with pathologic events (Shook et al., 2014), the characteristic mechanical stimulus in iNPH patients may induce further pathologic states in ventricular environments.

Hyper-dynamic CSF flow in iNPH patients, observed using PCMRI, significantly impacted flow dynamics associated with CSF flow mixing. In controls, the effects of CSF convection were moderate (Re ≈ 30), and the CSF flow profile had spatially uniform properties in the longitudinal direction. These moderate flow characteristics resulted in stable cyclic flow during pulsatile motion (Fig. 5). In contrast, the CSF flow in iNPH patients showed convection-dominant (Re ≈ 100) and non-negligible unsteady (Wo ≈ 2) profiles. Enhancement of the CSF mixing in the aqueduct associated with iNPH progression, as demonstrated in this study, has clinical and pathophysiological implications. Associations between CSF flow and neurological diseases have recently attracted attention from a biochemical perspective (Attier-Zmudka et al., 2019; Bothwell et al., 2019; Puy et al., 2016; Seo et al., 2021) and suggested associations between characteristic CSF flow alterations in iNPH patients and mixing of the CSF composition (Puy et al., 2016). Clinical studies reported that hyper-dynamic CSF flow through the aqueduct was associated with iNPH progression (Scollato et al., 2008) and this stabilization related to surgical outcomes (Shanks et al., 2019). Furthermore, MRI measurements of CSF flow dynamics using contrast agents revealed CSF mixing between the ventricle and subarachnoid space in iNPH

patients (Ringstad et al., 2017) and CSF flow stasis in the ventricle after shunt surgery (Kawaguchi et al., 2011). The obtained results are consistent with these clinical observations and thus indicate the significance of CSF flow dynamics in iNPH patients in CSF flow mixing from a fluid mechanics perspective. Therefore, we suggest that enhancement of the CSF mixing in the aqueduct in iNPH patients is not only a diagnostic criterion but also a possible factor that induces neurological symptoms associated with iNPH progression.

This study has three main limitations. First, the number of participants and their sex and age distributions were limited. However, because geometric and CSF flow differences between iNPH patients and controls were consistent with prior measurements (Bradley et al., 1996; Bradley, 2015), we believe the limited data did not critically affect the qualitative findings of our study. Nevertheless, further consideration using large population data should be conducted to provide a more comprehensive understanding of CSF flow characteristics. Second, this study considered CSF flow dynamics synchronized with cardiac pulsation measured using 4D flow MRI without considering other factors, such as respiratory motion, motile cilia, net CSF flow, and aqueduct wall motions. CSF flow measurements using other modalities have highlighted the influence of respiratory motion(Yamada et al., 2013), although the extent of its effect on CSF flow in the aqueduct remains controversial (Sincomb et al., 2020). Moreover, in vivo measurements of CSF dynamics using model animals showed motile cilia of ependymal cells present on the ventricle surfaces drive CSF flow (Faubel et al., 2016; Shook et al., 2014) to compartmentalize the CSF within individual ventricles (Olstad et al., 2019). Nevertheless, it remains unknown whether these findings from experimental studies in small animals can accurately model CSF pathophysiology in human ventricles (Ringers et al., 2020). In particular, global CSF flow in the ventricles can be

286 considered to be dominantly driven by the pulsatile motion related to the heartbeat, and the role
287 of the motile cilia seems to be localized in the near-wall flow field (Siyahhan et al., 2014). Further
288 investigations regarding the possible effects of motile cilia on CSF flow and mixing could address
289 the above question. In addition, net CSF flow through the aqueduct was not treated in this study
290 because it considered CSF flow over a relatively short period of at most 20 cardiac cycles.
291 Nevertheless, the net flow may affect the long-term CSF mixing states observed in biochemical
292 studies. Lastly, since the aqueduct wall motion cannot be detected in MRI with the voxel size of
293 the sub-mm scales, we assumed the aqueduct wall as rigid in computation. Although we believe
294 these effects are secondary on qualitative tendencies, wall motion may affect quantitative values,
295 especially the WSS, and subscale flow characteristics as well as primally cilia. Third, because of
296 limitations in spatiotemporal resolution, background noise, and artifacts in the 4D flow MRI, we
297 used the total CSF flow rate as a computational condition and did not assess the spatiotemporal
298 flow velocity map directly. Although 2D PCMRI with multiple slices can increase the
299 spatiotemporal resolution, we used 4D flow MRI because it can effectively detect complex CSF
300 movements in all three spatial directions in a limited scan time. Temporal resolution was limited
301 by the actual MRI scan time, which was chosen to minimize patient burden. The measurement
302 CSF flow profiles showed significant differences between controls and iNPH patients, consistent
303 with current understanding (Bradley, 2015), and thus we believe that the limited temporal
304 resolution did not affect the conclusions of this study. To address this issue, data assimilations
305 using MRI data (e.g, Otani et al., 2022) may be capable to obtain CSF flow characteristics in the
306 entire ventricles rather than just through the aqueducts.

In conclusion, this study investigated the biomechanical effects of the hyper-dynamic CSF flow through the aqueduct in iNPH patients using MRI-based computational simulations. CSF flow fields in the ventricles in 10 healthy controls and 10 iNPH patients were computed and mechanical stimuli and flow mixing states were evaluated. The obtained results demonstrated that iNPH causes high WSS values in relatively narrow regions of the aqueduct and significantly enhances the CSF flow mixing between ventricles. These findings suggest that hyper-dynamic CSF flow in iNPH results in significantly different fluid dynamical properties in the aqueduct in iNPH patients compared with healthy individuals and thus provide further insight into clinical and biological correlates of iNPH pathophysiology.

Appendix 1. Spatiotemporal validities of the 4D flow MRI

Validities of spatiotemporal resolution of 4D flow MRI data were confirmed from following two investigations. First, we evaluated spatial continuity of CSF flow rate through the aqueduct, as a validation of the spatial resolution. Time courses of the CSF flow rate during a cardiac cycle were extracted on representative four cross-sectional planes of the aqueduct and these average and standard deviation were evaluated in a control subject (control8) and an iNPH patient (iNPH8), as representatives (Fig. A1(A)). Standard variations were at most 5% of the average in both two cases, and thus we confirmed that the MRI data using in this study has acceptable spatial continuities of the CSF flow rate through the aqueduct. Next, we evaluated the net CSF flow and the CSF stroke volume through the aqueduct, as a validation of temporal resolution. Fig. A1 (B) shows the box plots of the net CSF flow and stroke volume through the aqueduct in one cardiac cycle in all healthy controls and iNPH patients. The net CSF flow volume

329 in controls and iNPH patients were 0.43±0.46 µl and 1.95±1.48 µl, respectively, and were at most
330 10% or less of this CSF stroke volume. Because the net CSF flow are negligibly small comparing to
331 the stroke volume (Bradley et al., 1996), these results are consistent with existing physiological
332 knowledge. From these validation studies, we concluded that the MRI data using in this study has
333 appropriate qualities to obtain the CSF flow rate through aqueducts.

334

335 **Appendix 2. Definition and computation of the mix-norm**

336 The mix-norm is an established multiscale measure of mixing (Mathew et al., 2005). In the
337 original definition, the mix-norm in the case of a one-dimensional torus

338 $S^1 = [0,1]$ is obtained by integrating the square of the average values of the function
339 $c : S^1 \to \mathbb{R}$ over a dense set of subsets contained in S^1. First, the mean value of c within the
340 interval $s \in (0,1)$ around $p \in [0,1]$ is given by

341 $$d(c, p, s) = \frac{1}{s} \int_{p-\frac{1}{2}}^{p+\frac{1}{2}} c(x)\mu(dx), \tag{4}$$

342 where μ is the Lebesgue measure. The mix-norm $\phi(c)$ is defined as the L^2 norm of the
343 function $d(c, p, s)$ averaged with respect to p and s, such that

344 $$\varphi(c, s) = \left(\int_{S^1} d^2(c, p, s)\mu(dp) \right)^{\frac{1}{2}}, \tag{5}$$

345 and then

$$\phi(c) = \left(\int_{S^1} \varphi^2(c,s)\mu(ds) \right)^{\frac{1}{2}}. \quad (6)$$

This definition was generalized to a multi-dimensional torus following a straightforward process (Mathew et al., 2005).

Arzani et al. (2014) used the mix-norm to evaluate the extent of discrete particle mixing in the domain of interest Γ from time t to $t+\Delta t$. First, they divided the domain Γ into equally-spaced subdomains $\Gamma_i\left(s_j\right)$ given by

$$\Gamma = \bigcup_{i=1}^{N_{s_j}} \Gamma_i(s_j), \quad (7)$$

where N_{s_j} is the total number of subdomains and s_j is the particular length scale used to form them. The function $c_i\left(s_j, \Delta t\right)$ was defined as the percentage of remaining particles in the region of interest in a finite time, such that

$$c_i(s_j, t+\Delta t) = \frac{N_{out}}{N_{in} + N_{out}}, \quad (8)$$

where N_{in} and N_{out} are the number of particles in $\Gamma_i\left(s_j\right)$ at time $t+\Delta t$ while inside and outside, respectively, at time t. Following the definitions in Eqs. (1)–(3), the mix-norm can be computed as the root mean square of c_i, as in the original definition. In the present study, we considered four different length scales to define s_j, which divided the aqueduct into 2, 4, 8, or 10 subdomains.

Supplementary material

Supplementary material 1: Inclusion criteria for iNPH patients and healthy controls

Supplementary material 2: Image acquisition details

Supplementary material 3: Geometric properties of the aqueduct and ventricles

Supplementary material 4: Mesh size independency test

Supplementary material 5: Computational details

Supplementary material 6: CSF stroke volume and peak wall shear stress in the aqueduct

Supplementary material 7: Video of particle tracking in the cerebral aqueduct of a healthy control

Supplementary material 8: Video of particle tracking in the cerebral aqueduct of an iNPH patient

Acknowledgments

We thank Edanz (https://jp.edanz.com/ac) for editing drafts of this manuscript. This work was supported by Grants-in-Aid for Scientific Research (19H01175 and 21K18037), and Grant-in-Aid for JSPS Fellows (23KJ1471) administered by the Japan Society for the Promotion of Science, the "Program for Promoting Researches on the Supercomputer Fugaku" (Project ID : hp220161) funded by the Ministry of Education, Culture, Sports, Science and Technology, and Multidisciplinary Research Laboratory System for Future Developments, Osaka University (No. 881100800).

Conflict of interest statement

The authors declare that the research was conducted in the absence of any commercial or financial relationships that could be construed as a potential conflict of interest.

5 References

Ambarki, K., Israelsson, H., Wåhlin, A., Birgander, R., Eklund, A., Malm, J., 2010. Brain ventricular size in healthy elderly: Comparison between evans index and volume measurement. Neurosurgery 67, 94–99. https://doi.org/10.1227/01.NEU.0000370939.30003.D1

Arzani, A., Les, A.S., Dalman, R.L., Shadden, S.C., 2014. Effect of exercise on patient specific abdominal aortic aneurysm flow topology and mixing. Int J Numer Method Biomed Eng 30, 280–295. https://doi.org/10.1002/cnm

Attier-Zmudka, J., Sérot, J.M., Valluy, J., Saffarini, M., Macaret, A.S., Diouf, M., Dao, S., Douadi, Y., Piotr Malinowski, K., Balédent, O., 2019. Decreased cerebrospinal fluid flow is associated with cognitive deficit in elderly patients. Front Aging Neurosci 11, 1–8. https://doi.org/10.3389/fnagi.2019.00087

Bazilevs, Y., Takizawa, K., Tezduyar, T.E., 2012. Computational fluid-structure interaction. John Wiley & Sons, Ltd. https://doi.org/10.1002/9781118483565

Bloomfield, I.G., Johnston, I.H., Bilston, L.E., 1998. Effects of proteins, blood cells and glucose on the viscosity of cerebrospinal fluid. Pediatr Neurosurg 28, 246–251. https://doi.org/10.1159/000028659

Bothwell, S.W., Janigro, D., Patabendige, A., 2019. Cerebrospinal fluid dynamics and intracranial pressure elevation in neurological diseases. Fluids Barriers CNS 16, 1–18. https://doi.org/10.1186/s12987-019-0129-6

Bradley, W.C., Scalzo, D., Queralt, J., Nitz, W.N., Atkinson, D.J., Wong, P., 1996. Normal-Pressure Hydrocephalus: Evaluation with Cerebrospinal Fluid Flow Measurements at MR Imaging. Radiology 198, 523–529.

Bradley, W.G., 2015. CSF Flow in the Brain in the Context of Normal Pressure Hydrocephalus. AJNR Am J Neuroradiol 36, 831–838. https://doi.org/10.3174/ajnr.A4124

Brinker, T., Stopa, E., Morrison, J., Klinge, P., 2014. A new look at cerebrospinal fluid circulation. Fluids Barriers CNS 11, 10. https://doi.org/10.1186/2045-8118-11-10

Cavanagh, M.E., Cornelis, M.E.P., Dziegielewska, K.M., Evans, C.A.N., Lorscheider, F.L., Møllgård, K., Reynolds, M.L., Saunders, N.R., 1983. Comparison of proteins in CSF of lateral and IVth ventricles during early development of fetal sheep. Developmental Brain Research 11, 159–167. https://doi.org/10.1016/0165-3806(83)90213-4

Damkier, H.H., Brown, P.D., Praetorius, J., 2013. Cerebrospinal fluid secretion by the choroid plexus. Physiol Rev 93, 1847–1892. https://doi.org/10.1152/physrev.00004.2013

Enzmann, D.R., Pelc, N.J., McComb, J.G., 1993. Cerebrospinal fluid flow measured by phase-contrast cine MR. American Journal of Neuroradiology 14, 1301-1307+1309.

Faubel, R., Westendorf, C., Bodenschatz, E., Eichele, G., 2016. Cilia-based flow network in the brain ventricles. Science (1979) 353, 176–178. https://doi.org/10.1126/science.aae0450

Kawaguchi, T., Hirata, Y., Bundo, M., Kondo, T., Owaki, H., Ito, S., Hashimoto, M., Ishikawa, M., 2011. Role of computerized tomographic cisternography in idiopathic normal pressure hydrocephalus. Acta Neurochir (Wien) 153, 2041–2048. https://doi.org/10.1007/s00701-011-1047-9

Lechtreck, K.F., Delmotte, P., Robinson, M.L., Sanderson, M.J., Witman, G.B., 2008. Mutations in Hydin impair ciliary motility in mice. Journal of Cell Biology 180, 633–643. https://doi.org/10.1083/jcb.200710162

Linninger, A.A., Tangen, K., Hsu, C.Y., Frim, D., 2016. Cerebrospinal Fluid Mechanics and Its Coupling to Cerebrovascular Dynamics. Annu Rev Fluid Mech 48, 219–257. https://doi.org/10.1146/annurev-fluid-122414-034321

Lun, M.P., Johnson, M.B., Broadbelt, K.G., Watanabe, M., Kang, Y.J., Chau, K.F., Springel, M.W., Malesz, A., Sousa, A.M.M., Pletikos, M., Adelita, T., Calicchio, M.L., Zhang, Y., Holtzman, M.J., Lidov, H.G.W., Sestan, N., Steen, H., Monuki, E.S., Lehtinen, M.K., 2015. Spatially heterogeneous

choroid plexus transcriptomes encode positional identity and contribute to regional CSF production. Journal of Neuroscience 35, 4903–4916. https://doi.org/10.1523/JNEUROSCI.3081-14.2015

Marmarou, A., Bergsneider, M., Relkin, N., Klinge, P., Black, P.M.L., 2005. INPH guidelines, part I: Development of guidelines for idiopathic normal-pressure hydrocephalus: Introduction. Neurosurgery 57. https://doi.org/https://doi.org/10.1227/01.NEU.0000168188.25559.0E

Mathew, G., Mezić, I., Petzold, L., 2005. A multiscale measure for mixing. Physica D 211, 23–46. https://doi.org/10.1016/j.physd.2005.07.017

May, C., Kaye, J.A., Atack, J.R., Schapiro, M.B., Friedland, R.P., Rapoport, S.I., 1990. Cerebrospinal fluid production is reduced in healthy aging. Neurology 40, 500–500. https://doi.org/10.1017/jfm.2020.463

Mori, E., Ishikawa, M., Kato, T., Kazui, H., Miyake, H., Miyajima, M., Nakajima, M., Hashimoto, M., Kuriyama, N., Tokuda, T., Ishii, K., Kaijima, M., Hirata, Y., Saito, M., Arai, H., 2012. Guidelines for management of idiopathic normal pressure hydrocephalus: Second edition. Neurol Med Chir (Tokyo) 52, 775–778. https://doi.org/10.2176/nmc.52.775

Nakajima, M., Yamada, S., Miyajima, M., Ishii, K., Kuriyama, N., Kazui, H., Kanemoto, H., Suehiro, T., Yoshiyama, K., Kameda, M., Kajimoto, Y., Mase, M., Murai, H., Kita, D., Kimura, T., Samejima, N., Tokuda, T., Kaijima, M., Akiba, C., Kawamura, K., Atsuchi, M., Hirata, Y., Matsumae, M., Sasaki, M., Yamashita, F., Aoki, S., Irie, R., Miyake, H., Kato, T., Mori, E., Ishikawa, M., Date, I., Arai, H., 2021. Guidelines for management of idiopathic normal pressure hydrocephalus (Third edition): Endorsed by the Japanese society of normal pressure hydrocephalus. Neurol Med Chir (Tokyo) 61, 63–97. https://doi.org/10.2176/nmc.st.2020-0292

Nicholson, C., 1999. Signals that go with the flow. Trends Neurosci 22, 143–145. https://doi.org/10.1016/S0166-2236(98)01388-5

Olstad, E.W., Ringers, C., Hansen, J.N., Wens, A., Brandt, C., Wachten, D., Yaksi, E., Jurisch-Yaksi, N., 2019. Ciliary Beating Compartmentalizes Cerebrospinal Fluid Flow in the Brain and Regulates Ventricular Development. Current Biology 29, 229-241.e6. https://doi.org/10.1016/j.cub.2018.11.059

Otani, T., Yamashita, H., Iwata, K., Ilik, S.Y., Yamada, S., Watanabe, Y., Wada, S., 2022. A concept on velocity estimation from magnetic resonance

velocity images based on variational optimal boundary control. Journal of Biomechanical Science and Engineering 22–00050. https://doi.org/10.1299/jbse.22-00050

Puy, V., Zmudka-Attier, J., Capel, C., Bouzerar, R., Serot, J.M., Bourgeois, A.M., Ausseil, J., Balédent, O., 2016. Interactions between flow oscillations and biochemical parameters in the cerebrospinal fluid. Front. Aging Neurosci. 8, 1–8. https://doi.org/10.3389/fnagi.2016.00154

Ringers, C., Olstad, E.W., Jurisch-Yaksi, N., 2020. The role of motile cilia in the development and physiology of the nervous system. Philosophical Transactions of the Royal Society B: Biological Sciences 375. https://doi.org/10.1098/rstb.2019.0156

Ringstad, G., Vatnehol, S.A.S., Eide, P.K., 2017. Glymphatic MRI in idiopathic normal pressure hydrocephalus. Brain 140, 2691–2705. https://doi.org/10.1093/brain/awx191

Scollato, A., Tenenbaum, R., Bahl, G., Celerini, M., Salani, B., Di Lorenzo, N., 2008. Changes in aqueductal CSF stroke volume and progression of symptoms in patients with unshunted idiopathic normal pressure hydrocephalus. American Journal of Neuroradiology 29, 192–197. https://doi.org/10.3174/ajnr.A0785

Seo, J.S., Mantas, I., Svenningsson, P., Greengard, P., 2021. Ependymal cells-CSF flow regulates stress-induced depression. Mol Psychiatry 26, 7308–7315. https://doi.org/10.1038/s41380-021-01202-1

Shanks, J., Markenroth Bloch, K., Laurell, K., Cesarini, K.G., Fahlström, M., Larsson, E.M., Virhammar, J., 2019. Aqueductal CSF stroke volume is increased in patients with idiopathic normal pressure hydrocephalus and decreases after shunt surgery. American Journal of Neuroradiology 40, 453–459. https://doi.org/10.3174/ajnr.A5972

Shook, B.A., Lennington, J.B., Acabchuk, R.L., Halling, M., Sun, Y., Peters, J., Wu, Q., Mahajan, A., Fellows, D.W., Conover, J.C., 2014. Ventriculomegaly associated with ependymal gliosis and declines in barrier integrity in the aging human and mouse brain. Aging Cell 13, 340–350. https://doi.org/10.1111/acel.12184

Sincomb, S., Coenen, W., Sánchez, A.L., Lasheras, J.C., 2020. A model for the oscillatory flow in the cerebral aqueduct. J Fluid Mech. https://doi.org/10.1017/jfm.2020.463

Siyahhan, B., Knobloch, V., De Zélicourt, D., Asgari, M., Daners, M.S., Poulikakos, D., Kurtcuoglu, V., 2014. Flow induced by ependymal cilia dominates near-wall cerebrospinal fluid dynamics in the lateral ventricles. J R Soc Interface 11. https://doi.org/10.1098/rsif.2013.1189

Skipor, J., Thiery, J.C., 2008. The choroid plexus - cerebrospinal fluid system: Undervaluated pathway of neuroendocrine signaling into the brain. Acta Neurobiol Exp (Wars) 68, 414–428.

Sotelo, J., Urbina, J., Valverde, I., Tejos, C., Irarrázaval, P., Hurtado, D.E., Uribe, S., 2015. Quantification of wall shear stress using a finite-element method in multidimensional phase-contrast MR data of the thoracic aorta. J Biomech 48, 1817–1827. https://doi.org/10.1016/j.jbiomech.2015.04.038

Sweetman, B., Xenos, M., Zitella, L., Linninger, A.A., 2011. Three-dimensional computational prediction of cerebrospinal fluid flow in the human brain. Comput Biol Med 41, 67–75. https://doi.org/10.1016/j.compbiomed.2010.12.001

Wentland, A.L., Wieben, O., Korosec, F.R., Haughton, V.M., 2010. Accuracy and reproducibility of phase-contrast MR imaging measurements for CSF flow. American Journal of Neuroradiology 31, 1331–1336. https://doi.org/10.3174/ajnr.A2039

Yamada, S., Ishikawa, M., Ito, H., Yamamoto, K., Yamaguchi, M., Oshima, M., Nozaki, K., 2020. Cerebrospinal fluid dynamics in idiopathic normal pressure hydrocephalus on four-dimensional flow imaging. Eur Radiol 30, 4454–4465. https://doi.org/10.1007/s00330-020-06825-6

Yamada, S., Ito, H., Ishikawa, M., Yamamoto, K., Yamaguchi, M., Oshima, M., Nozaki, K., 2021. Quantification of Oscillatory Shear Stress from Reciprocating CSF Motion on 4D Flow Imaging. American Journal of Neuroradiology 1–8. https://doi.org/10.3174/ajnr.a6941

Yamada, S., Miyazaki, M., Yamashita, Y., Ouyang, C., Yui, M., Nakahashi, M., Shimizu, S., Aoki, I., Morohoshi, Y., Mccomb, J.G., 2013. Influence of respiration on cerebrospinal fluid movement using magnetic resonance spin labeling. Fluids Barriers CNS 10, 1–7. https://doi.org/10.1186/2045-8118-10-36

Yavuz Ilik, S., Otani, T., Yamada, S., Watanabe, Y., Wada, S., 2022. A subject-specific assessment of measurement errors and their correction in cerebrospinal fluid velocity maps using 4D flow MRI. Magn Reson Med 87, 2412–2423. https://doi.org/10.1002/mrm.29111

559 Zappaterra, M.D., Lisgo, S.N., Lindsay, S., Gygi, S.P., Walsh, C.A., Ballif, B.A.,
560 2007. A comparative proteomic analysis of human and rat embryonic
561 cerebrospinal fluid. J Proteome Res 6, 3537–3548.
562 https://doi.org/10.1021/pr070247w

563 Zhangyang, W., Yiying Zhang, Fan Hu, Jing Ding, Xin Wang, 2020.
564 Pathogenesis and pathophysiology of idiopathic normal pressure
565 hydrocephalus. CNS Neurosci Ther 1230–1240.
566 https://doi.org/10.1111/cns.13526

567 Zhou, X., Xia, J., 2022. Application of Evans Index in Normal Pressure
568 Hydrocephalus Patients: A Mini Review. Front Aging Neurosci.
569 https://doi.org/10.3389/fnagi.2021.783092

570

571

572 Table 1 Basal geometric properties of all subjects (Left ventricle: LV, Third ventricle: 3V, Fourth
573 ventricle: 4V). Evans index is used to evaluate ventriculomegaly, and hydrocephalus is defined
574 as > 0.3 (Nakajima et al., 2021).

Case	LV volume [ml]	3V volume [ml]	4V volume [ml]	Evans index
control1	37.4	1.6	2.6	0.276
control2	27.4	1.4	1.6	0.254
control3	18.3	1.1	1.6	0.240
control4	18.9	1.3	2.2	0.249
control5	19.6	1.0	1.7	0.259
control6	10.8	1.3	1.9	0.221
control7	17.2	1.5	1.9	0.255
control8	24.3	0.7	1.4	0.270
control9	7.2	0.8	0.9	0.236
control10	16.7	0.9	1.4	0.225
iNPH1	138.8	4.3	2.5	0.373
iNPH2	104.4	3.9	2.6	0.329
iNPH3	99.7	4.5	3.5	0.329
iNPH4	104.6	6.4	2.5	0.301
iNPH5	61.7	2.4	1.6	0.301
iNPH6	71.9	4.0	1.9	0.318
iNPH7	152.5	6.0	4.7	0.384
iNPH8	165.9	5.0	4.2	0.342
iNPH9	114.2	4.1	4.4	0.332
iNPH10	83.5	4.8	2.2	0.373

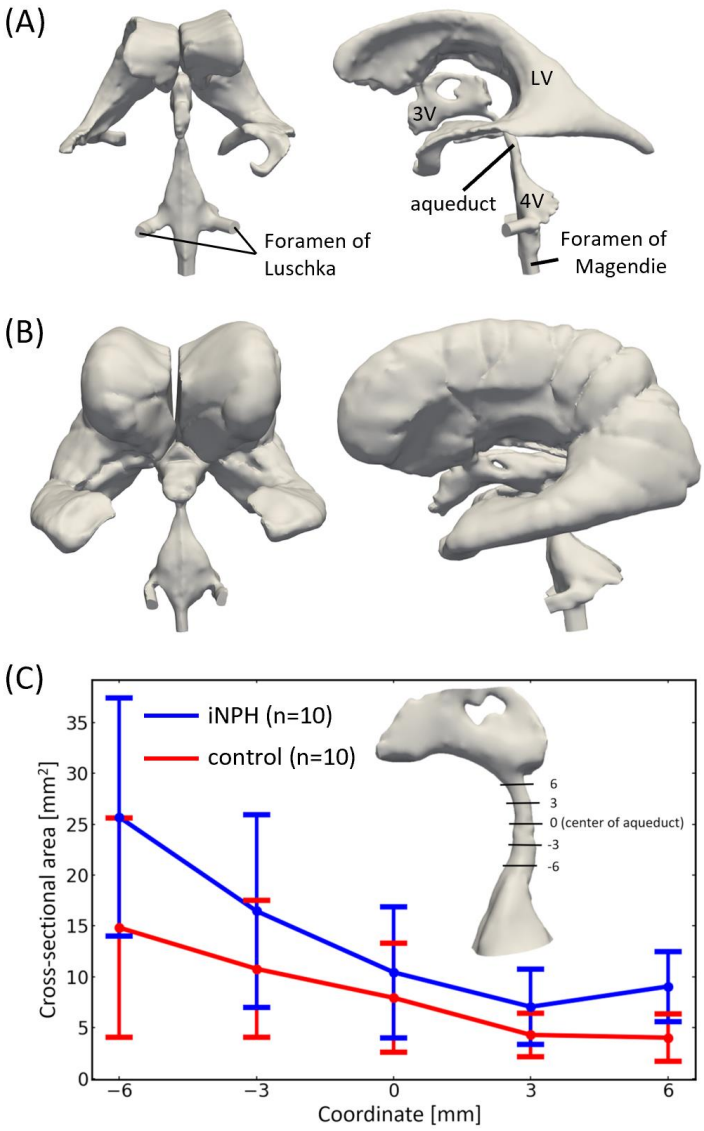

Fig. 1. Geometries of the cerebral ventricles of a healthy control (A) and an idiopathic normal pressure hydrocephalus (iNPH) patient (B), reconstructed from T2-weighted magnetic resonance images, and the cross-sectional area of the cerebral aqueduct (mean ± S.D.) along its length (C) in healthy controls (red line) and iNPH patients (blue line).

LV: lateral ventricle, 3V: third ventricle, 4V: fourth ventricle.

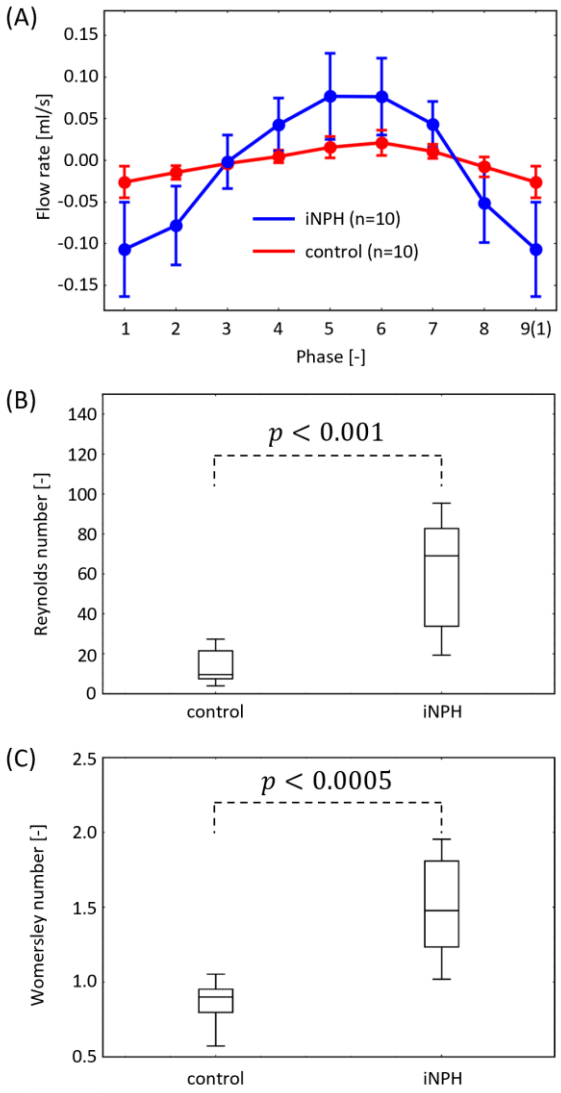

582

583 Fig. 2. Time course of the cerebrospinal fluid (CSF) flow rate through the aqueduct (A) in healthy
584 controls and iNPH patients (mean ± S.D.). Maximum Reynolds number on the cross-sectional
585 plane in the aqueduct (B) and associated Womersley number (C). A Mann–Whitney *U* test was
586 used to compute *p* values.

587

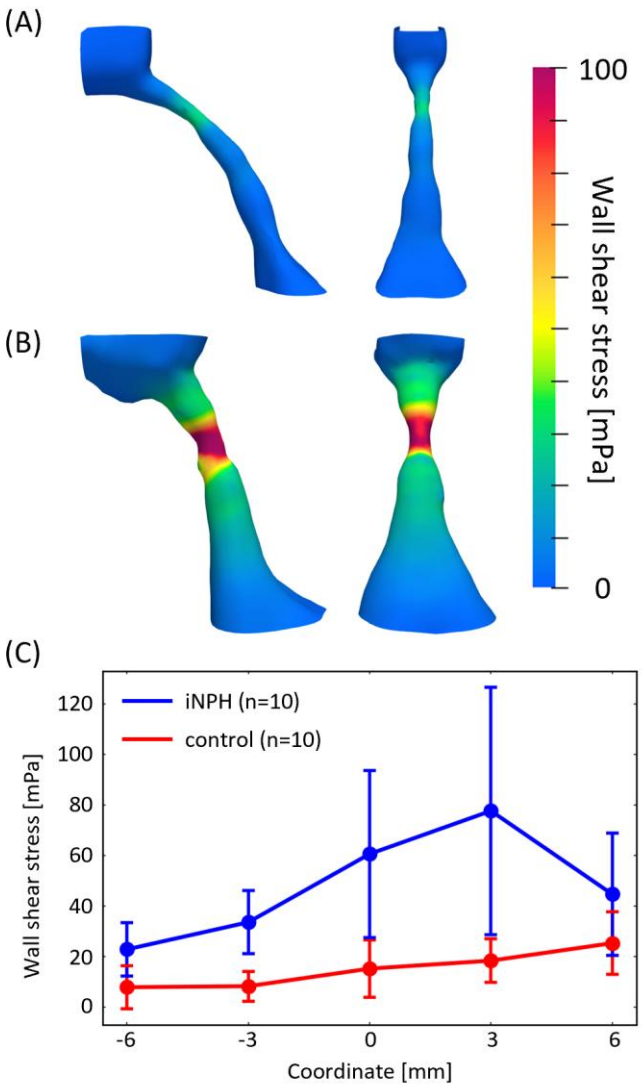

588

589 Fig. 3. Wall shear stress distributions on the cerebral aqueduct wall in a representative healthy
590 control (A) and iNPH patient (B), and wall shear stress distributions in the aqueduct (mean ± S.D.)
591 along its length (C) in healthy controls (red line) and iNPH patients (blue line). The definition of
592 the coordinate is the same as that in Fig. 1 (C).

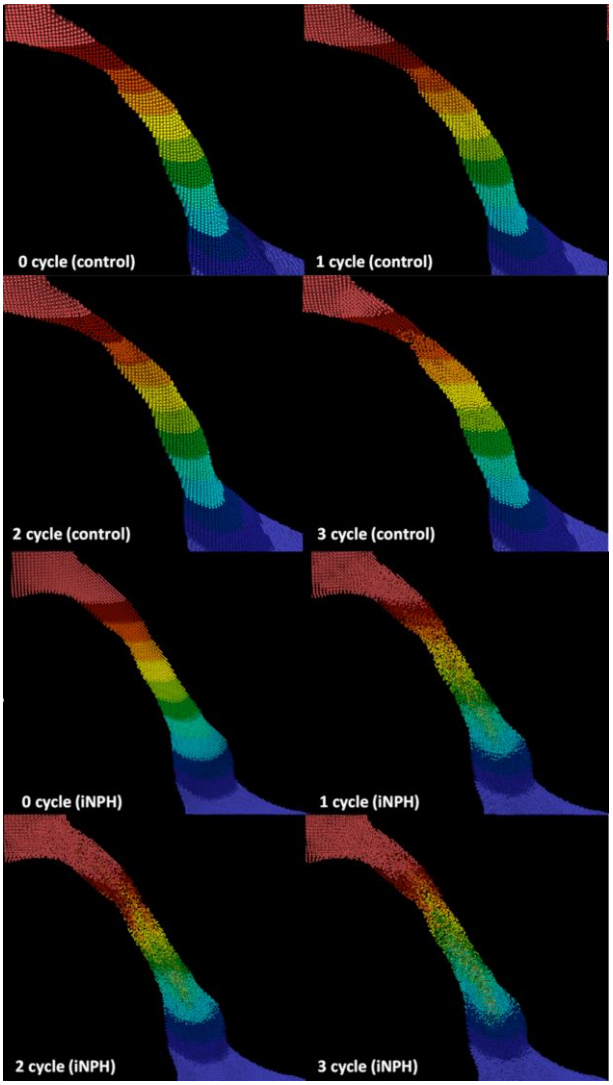

Fig. 4. Time course of the three-dimensional particle tracer distributions in the cerebral aqueduct in a representative healthy control (top) and iNPH patient (bottom) in the left-side view. The color of the particle tracer is set according to its initial position. Videos of the time course are shown in Electronic supplementary material 7 (control) and 8 (iNPH).

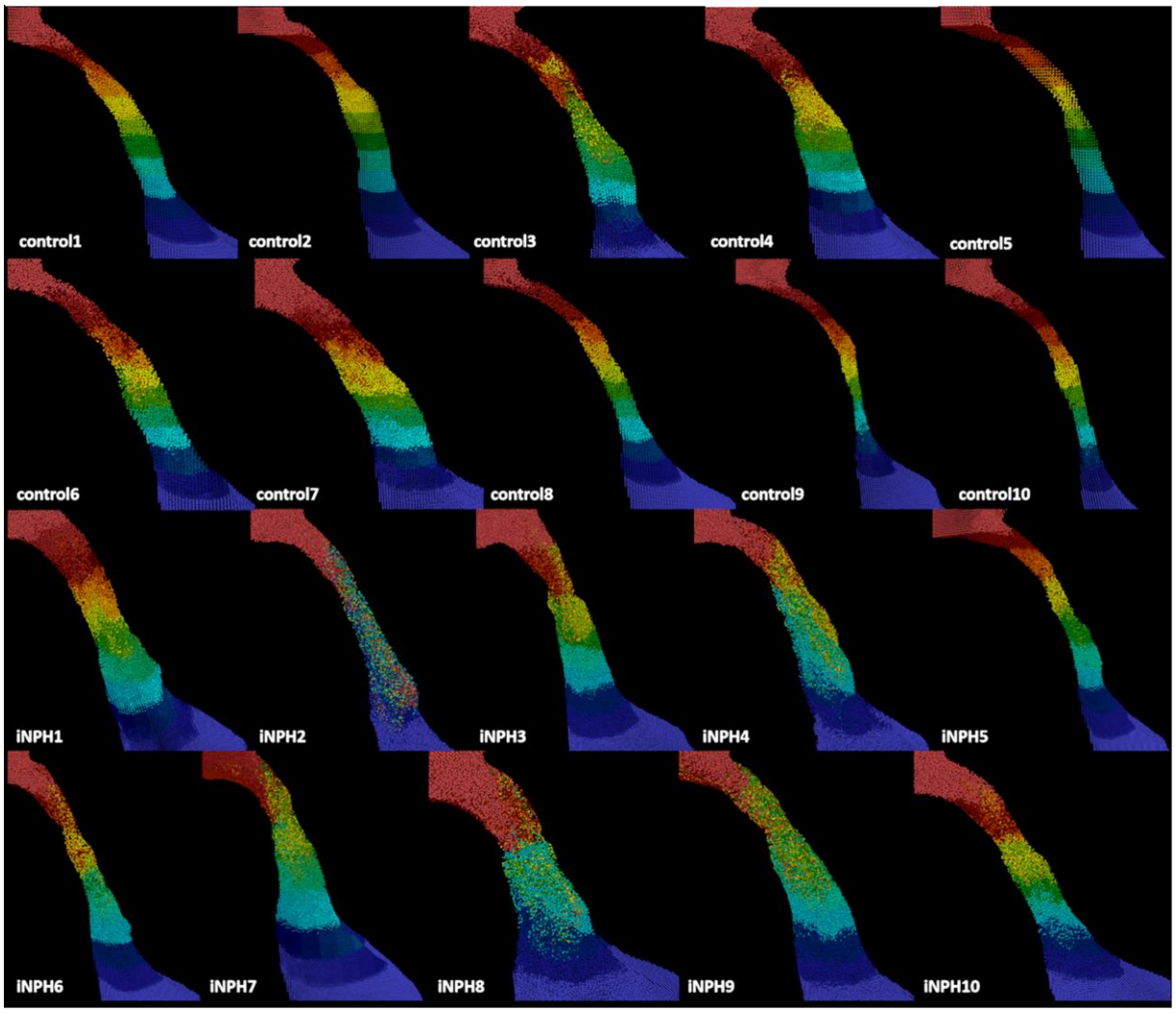

599

600 Fig. 5. Three-dimensional particle tracer distributions in the cerebral aqueduct after 20 cardiac
601 cycles in healthy controls (top) and iNPH patients (bottom) in the left-side view.

602

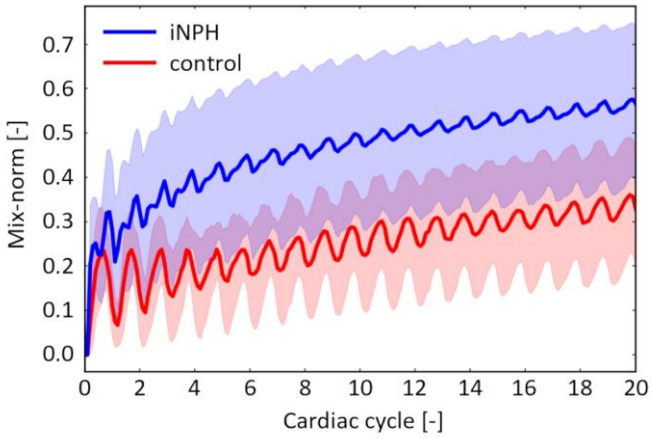

603

604 Fig. 6. Time course of the average mix-norm in the cerebral aqueduct in healthy controls (red)

605 and iNPH patients (blue). The shaded area represents the standard deviation.

606

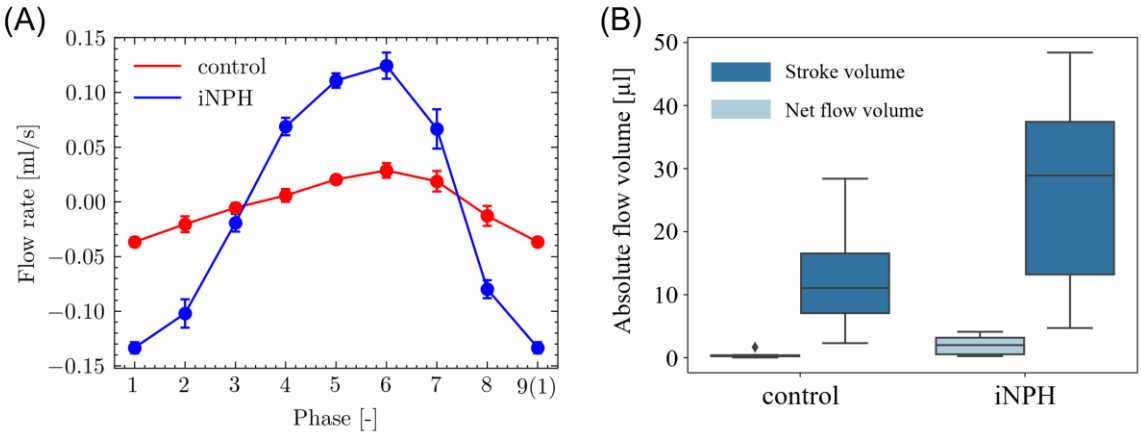

Fig. A1 (A) Time courses of the cerebrospinal fluid (CSF) flow rate (mean ± S.D.) among four cross-sectional planes in the aqueduct in a representative control (red) and an iNPH patient (blue) and (B) box plots of net CSF flow volume and stroke volume for a cardiac cycle in all healthy controls (left) and iNPH patients (left).